Fast Neutron Scatter Imager for Proton Range Monitoring in Hadron Therapy: First Experimental Results

Dowon Lee[1], Hayoung Sim[2], Jimin Shin[1], Hee Seo[1*]

[1]Department of Applied Plasma and Quantum Beam Engineering, Jeonbuk National University, Jeonju 54896, Republic of Korea

[2]Department of Radiation Regulation Management, Korea Institute of Nuclear Safety (KINS), Daejeon 34142, Republic of Korea

ABSTRACT

Accurate *in-vivo* beam range verification is crucial for both maximization of therapeutic benefits and minimization of normal-tissue complications in hadron therapy. This study presents the first experimental proof-of-concept for proton beam range monitoring utilizing a prototype fast neutron scatter imager. The imaging system consists of 4×4 arrays of stilbene and EJ-276 organic scintillators coupled to silicon photomultipliers (SiPMs) with a multiplexed readout. At the National Cancer Center in the Republic of Korea, a clinical proton beam with four discrete energy levels (102.71, 152.09, 202.36, and 221.86 MeV) irradiated a tissue-equivalent PMMA phantom. By applying a list-mode maximum likelihood expectation maximization (LM-MLEM) algorithm, the spatial distributions of secondary neutrons were successfully reconstructed from double-scatter events. The reconstructed images clearly visualized the macroscopic secondary-neutron distribution and the distinct dose fall-off region preceding the proton's Bragg peak. Notably, the energy-dependent spatial shifts of the neutron production position were accurately captured, which results strongly aligned with Geant4 Monte Carlo simulations. Although the current geometric efficiency and temporal processing bottlenecks limited the overall event yield, the present study's qualitative localization of the Bragg peak successfully demonstrates, for the first time, the fundamental feasibility of fast neutron scatter imaging. With planned hardware upgrades, this approach will pave the way for a robust, real-time *in-vivo* range verification system applicable to advanced heavier ion treatments such as carbon ion therapy.

Keywords: Proton Beam Therapy, Beam Range, Fast Neutron Scatter Imaging, Image Reconstruction

*Corresponding author: hseo@jbnu.ac.kr

1. Introduction

In recent years, the overall cancer diagnostic rate has continued to rise, driving the development of more precise and effective treatment modalities. Among these, heavy particle therapy (also called hadron therapy) has emerged as a promising approach that exploits the Bragg peak characteristics of heavy ion beams to deliver a highly conformal dose to malignant tumors while minimizing radiation exposure of surrounding normal tissues [1–3]. This inherent advantage offers improved local tumor control with reduced normal-tissue complications compared with conventional photon-based radiotherapy. However, the therapeutic benefit of heavy particle therapy critically depends on the spatial accuracy of dose delivery. If the dose is delivered to an incorrect position, the tumor may not be adequately destroyed or may be at higher risk of recurrence, while damage to surrounding normal tissues and organs can increase dramatically. Dosimetric phantom-based QA/QC, which can detect geometric deviations to the millimeter level, enables precise verification of dose delivery accuracy [4,5]. However, setup uncertainties arise from beam/anatomy misalignment and internal tissue heterogeneity variations [6]. These uncertainties can lead to deviations in the actual beam range from the planned values, potentially compromising the accuracy of dose delivery to the target volume [7]. Although Radiation Therapy Planning (RTP) systems incorporate these effects using photon computed tomography (CT) imaging, uncertainties in CT Hounsfield Units (HU)-to-stopping power conversion limit calculation accuracy [8]. Consequently, accurate beam range measurement is essential during treatment, and research on *in-vivo* range verification methods capable of directly assessing the delivered beam inside the patient is actively ongoing [9,10].

During treatment, secondary particles generated from beam/tissue interactions provide valuable information for monitoring and verification of the delivered dose. Although these secondary particles contribute to additional unwanted dose deposition and radiation burden [11,12], they also serve as informative signals that reflect the beam's transport and interaction history within tissue. In particular, prompt gamma rays emitted along the beam path have been widely investigated for range verification, enabling non-invasive assessment of the actual particle range [13,14]. Likewise, secondary neutrons produced by nuclear interactions can carry information on the beam trajectory and interaction sites, making them a potential signal source for reconstructing the spatial distribution of the neutron source and indirectly inferring the beam's *in-vivo* behavior. Recently, hybrid multi-particle approaches that simultaneously utilize both prompt gammas and secondary neutrons also have been proposed as means of maximizing verification accuracy [15]. This trend further underscores the growing importance of precisely mapping the secondary-neutron distribution.

Accordingly, this study explored the application of fast neutron scatter imaging for accurate mapping of the secondary-neutron distribution. Our ultimate clinical objective is to develop a robust, real-time range verification system for heavier particle treatments, such as carbon ion therapy. Compared with proton therapy, heavier ions undergo more extensive nuclear interactions—specifically, both target and projectile fragmentation—resulting in a significantly

higher yield of secondary neutrons [16,17]. While this elevated neutron production contributes to out-of-field secondary doses that necessitate strict monitoring, it simultaneously provides a much higher and more robust signal flux for fast neutron scatter imagers. Therefore, as the first evaluation of our prototype system in a proton beam environment, this work serves as a foundational and rigorous proof-of-concept validation of the pertinent operational principles and reconstruction algorithms prior to extending the application to carbon ion therapy.

2. Materials and Methods

2.1. Principle of Fast Neutron Scatter Imaging

Fast neutron scatter imaging relies on the kinematics of elastic scattering between incident neutrons and protons (n-p scattering) within hydrogen-rich organic scintillators. When a fast neutron from a source interacts with the front detector (Detector 1) and subsequently scatters into the rear detector (Detector 2), a double-scatter event is recorded. By measuring the energy deposited by the recoil proton in the first detector (E_p) and the scattering position and interaction time within both detectors, the scattering angle (θ) can be calculated assuming n-p elastic scattering and non-relativistic kinematics:

$$E_{n'} = \frac{1}{2} m_n \left(\frac{\overline{p_1 p_2}}{\mathrm{TOF}}\right)^2 \tag{2.1}$$

$$\theta = \arctan\left(\frac{E_p}{E_{n'}}\right) \tag{2.2}$$

Here, $E_{n'}$ and E_p represent the kinetic energies of the scattered neutron and the recoil proton, respectively. $E_{n'}$ is determined by its time-of-flight (TOF) and the distance ($\overline{p_1 p_2}$) between the two scattering interactions, where m_n is the rest mass of the neutron. This scattering angle θ defines a "probability cone." The apex of this cone is located at the interaction position in Detector 1, and its central axis is aligned with the vector connecting the interaction points in Detectors 1 and 2. The original neutron source is constrained to lie somewhere on the surface of this cone, as illustrated in Fig. 1. By accumulating multiple valid double-scatter events, the overlapping probability cones converge at the true spatial location of the neutron source.

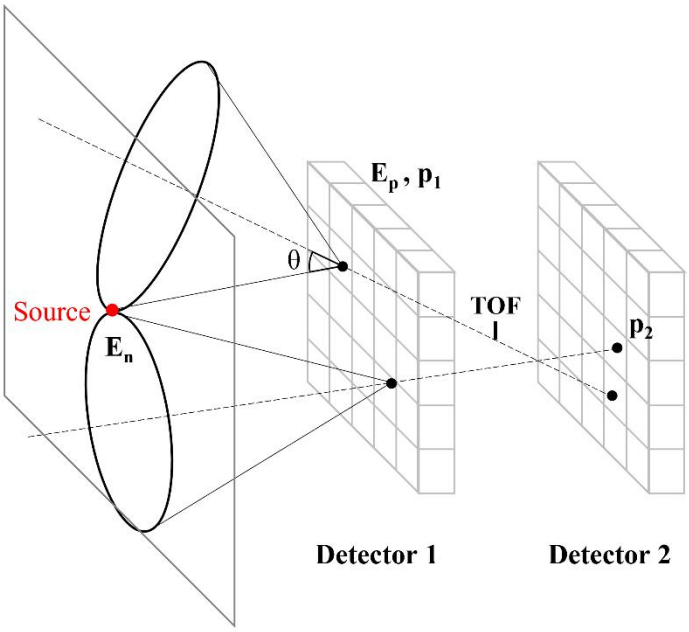

Fig. 1. Schematic principle of fast neutron scatter imaging. A valid double-scatter event defines a probability cone with a scattering angle (θ) determined by the recoil proton energy (E_p) and time-of-flight (TOF). The cone's apex is located at the first interaction position (p_1) in Detector 1, and its axis aligns with the vector connecting the interaction points in Detector 1 and Detector 2 (p_2).

To reconstruct the spatial distribution of the neutron source from the collected overlapping cones, advanced image reconstruction algorithms are required. Simple Back Projection (SBP) can provide a basic estimate by simply superimposing the probability cones in the imaging space; however, it often suffers from severe blurring and artifacts, particularly when the number of valid events is limited [18, 19]. To overcome these limitations and achieve higher spatial resolution, an iterative reconstruction algorithm, specifically List-Mode Maximum Likelihood Expectation Maximization (LM-MLEM), was employed in this study [18]. Unlike conventional MLEM, which aggregates data into predefined spatial bins, LM-MLEM processes each scattering event individually in an event-by-event manner. This event-by-event approach is particularly advantageous for sparse data sets with low event yields [20,21]. By iteratively maximizing the likelihood function while incorporating the geometric system matrix and detector resolution parameters (i.e., energy, time, and position resolution), LM-MLEM can effectively suppress background noise and provide a more distinct reconstruction of the neutron source distribution.

2.2. Experimental Setup

The prototype fast neutron scatter imager employed in this study was constructed using 4×4 arrays of organic scintillators (stilbene and EJ-276), each pixel measuring 3×3×10 mm^3. These scintillator arrays were optically coupled to Hamamatsu 4×4 array silicon photomultipliers (SiPMs, S13361-3050AE-04) using EJ-550 optical grease. To optimize system performance, the stilbene array was positioned in front of the EJ-276 array, as stilbene crystals exhibit better energy resolution [22]. The output signals from the SiPMs were processed and amplified utilizing AiT's dedicated 4-channel active base readout boards (AB4HFN-S133613004), as shown in Fig. 2. Subsequently, the signals were transmitted to a CAEN multichannel digitizer (V1730SB) for analog-to-digital conversion. Final data acquisition was managed by the CAEN CoMPASS software, which recorded the digital data transmitted via a CAEN A4818 optical controller. Energy thresholds of 47.9 keVee and 36.1 keVee were applied to the stilbene and EJ-276 detectors, respectively, to reject events below the electronic noise floor of each channel.

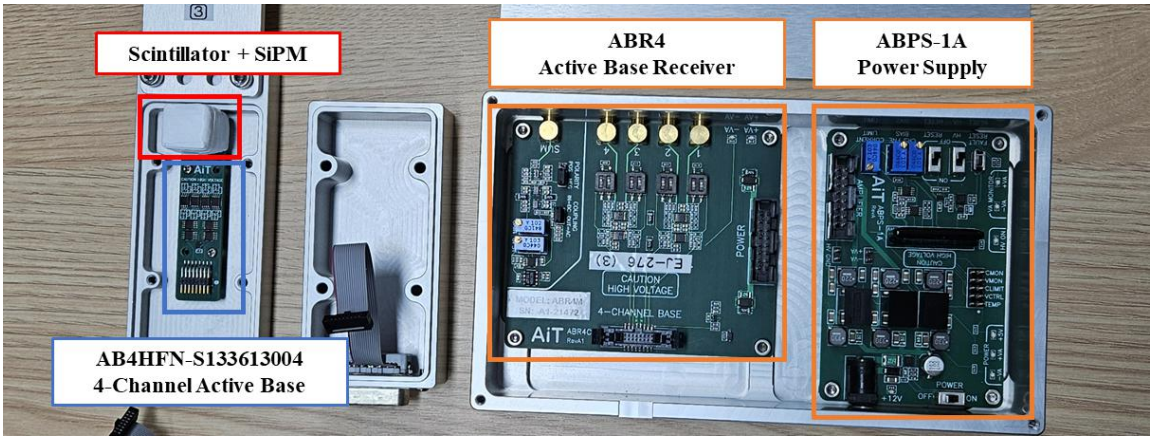

Fig. 2. Photographs of prototype detector module and its dedicated readout electronics. The setup consists of a 4×4 scintillator array coupled to a SiPM with an integrated 4-channel active base (left), an active base receiver for signal processing (center), and a dedicated power supply unit (right).

Following data acquisition, double-scatter event matching and subsequent image reconstruction were executed using custom-developed Python code. To select valid neutron double-scatter events from the raw dataset, a specific time-of-flight (TOF) window (0.1 ns < TOF < 100 ns) was applied for coincidence detection logic and exclusion of gamma events. Exclusively from these extracted valid events, the final neutron scattering images were then reconstructed.

The experiment was conducted in a fixed-beam treatment room using the IBA Proteus 235 cyclotron (Ion Beam Applications, Louvain-la-Neuve, Belgium) installed at the National Cancer Center (NCC) in Korea, which can accelerate protons up to 230 MeV. The fixed-beam treatment system was operated in double-scattering mode [23]; however, the second scatterer and range modulator were set to the open (hole) position, so that the beam passed through

the first scatterer only. This configuration produced a narrower spot size and a nearly monoenergetic energy spectrum relative to the standard double-scattering mode, thus approximating the characteristics of a pencil beam.

Under normal clinical operating conditions, the extracted beam current can reach up to 300 nA; however, transmission through the Energy Selection System (ESS), which employs a graphite degrader and collimating slits, significantly attenuates the beam, constraining the current at the treatment room to below 20 nA [24–26]. For this study, the extracted beam current was set substantially lower than typical clinical levels in order to maintain a low-flux condition and prevent signal pile-up in the multiplexed readout system of our prototype detector. Furthermore, since the ESS's transmission efficiency varies significantly with beam energy, the cyclotron current was carefully adjusted for each energy setting to consistently maintain the desired low-event-rate environment. The specific beam current values for each energy are listed in Table 1.

A 100 × 100 × 400 mm^3 tissue-equivalent PMMA phantom was used as the target. Since the standard beam range data for each energy was based on a water phantom, the actual beam range within the PMMA was approximated in this experiment by applying a depth scaling factor for PMMA [27]. The detector was positioned 10 cm from the lateral surface of the phantom. The distance between the detectors was 3 cm. Due to the limited volume of the detector, the reconstructable field of view (FOV) for the imaging system was inherently restricted. To compensate for this limitation and accurately observe the dose fall-off, the detector was strategically positioned at the expected proton range (Bragg peak) prior to each measurement.

For energy calibration, the light output of the organic scintillation detector was calibrated in electron equivalent energy (MeVee) units using a Cs-137 point source (17.78 μCi), as shown in Fig. 3. The calibration was carried out by comparing the Compton continuum in the measured spectrum with that of simulated spectra generated with energy resolutions ranging from 15 to 25%. The simulated spectra were post-processed using Python code to produce a range of spectra corresponding to different gain values, and the optimal match to the measured Compton continuum was identified for energy calibration of each detector. Subsequently, an empirical light output function for stilbene crystals was applied to convert the calibrated electron equivalent energy into proton energy (MeV) [28]. Additionally, to reduce prompt gamma events, lead shielding of 2.5 cm thickness was positioned around the detector. The experimental setup and DAQ system are shown in Fig. 4.

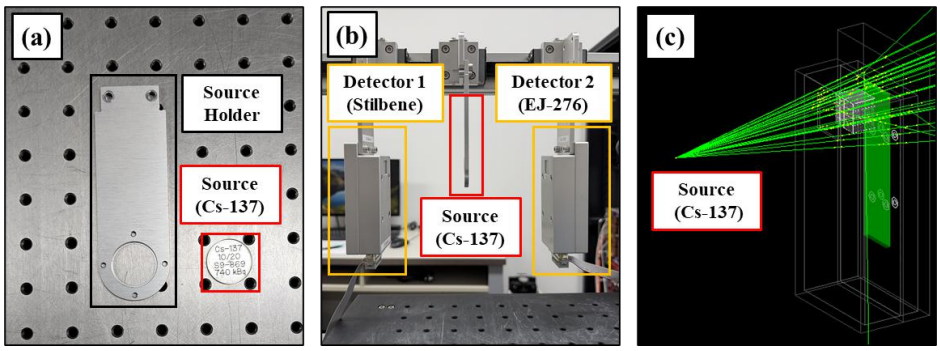

Fig. 3. Photographs of energy calibration setup: (a) source holder with Cs-137 point source (17.78 μCi); (b) measurement configuration showing Cs-137 source positioned between Detector 1 (Stilbene) and Detector 2 (EJ-276); and (c) corresponding Geant4 simulation geometry replicating the setup

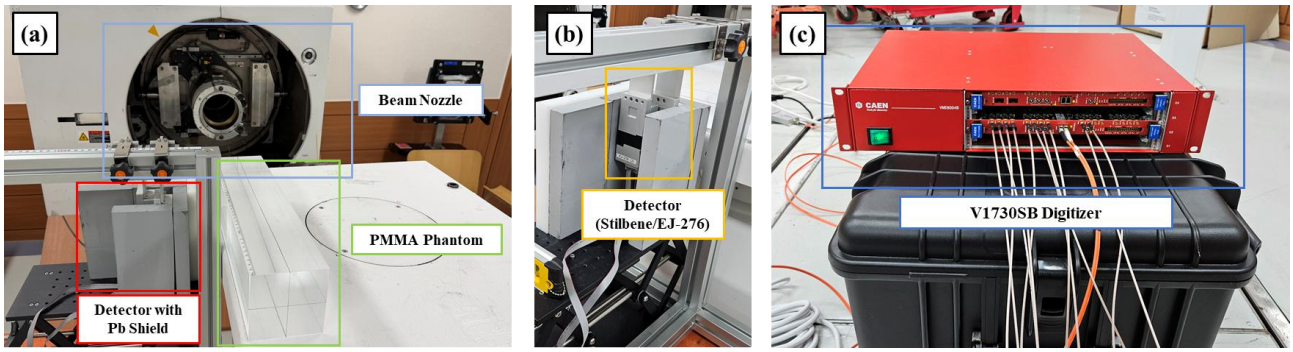

Fig. 4. Photographs of experiment setup: (a) overall arrangement in treatment room showing proton beam nozzle, PMMA phantom, and detectors with lead shielding; (b) close-up view of prototype fast neutron scatter imager (Stilbene/EJ-276 arrays) positioned within lead blocks; and (c) DAQ system featuring CAEN V1730SB multichannel digitizer

Table 1. Proton beam configurations

Energy (MeV)	PMMA Range (cm)	Cyclotron Current (nA)	Measurement Time (s)
102.71	7.00	10	1080
152.09	14.00	1	300
202.36	22.88	0.1	210
221.86	26.74	0.1	180

2.3. Secondary-neutron Distribution

To estimate the spatial distribution of secondary neutrons within the PMMA phantom, Monte Carlo simulations were performed using the Geant4 toolkit (version 11.3.2) with the QGSP_BIC_HP physics list [29]. A PMMA phantom, its dimensions identical to those used in the physical experiment, was modeled and irradiated with a simulated proton

beam. To ensure a direct comparison with the experimental data, the incident beam was configured using proton energies, their corresponding spot size matching those used in the experiment. The specific spot size values for each energy level were adopted from the measurements presented in Cho et al.'s ETRI report [30]. Although this approach served as an approximation based on the available PBS (pencil beam scanning) data, preliminary simulations confirmed that variations in spot size did not significantly affect the depth-dose distribution or secondary-neutron distribution along the beam axis, which are the primary quantities of interest for beam range monitoring. The resulting secondary-neutron distributions and the corresponding depth-dose distribution for each energy level are illustrated in Fig. 5.

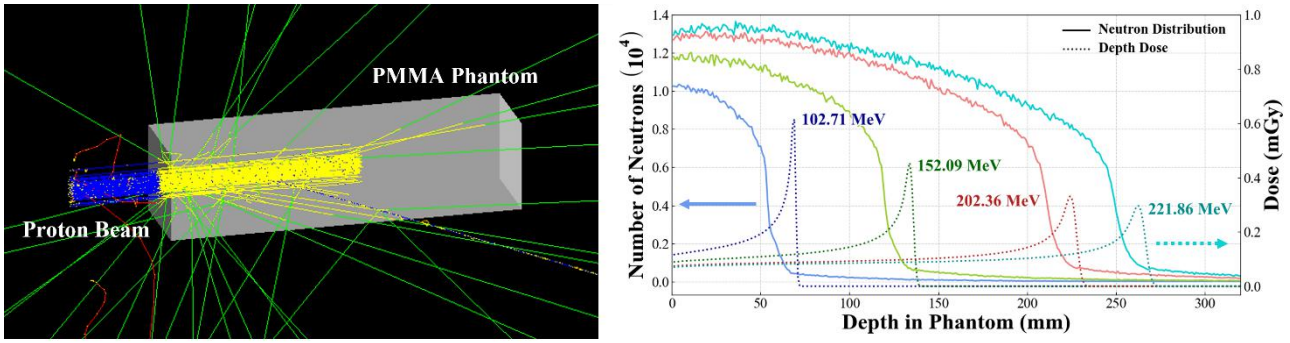

Fig. 5. Monte Carlo simulation of secondary-neutron distribution. (a) Geant4 simulation model of proton beam incident on PMMA phantom. (b) Simulated depth profiles of secondary-neutron distribution (solid lines) and dose deposition (dotted lines) for varying proton beam energies.

3. Results and Discussion

The data acquired from the proton beam test at four discrete energy levels (102.71, 152.09, 202.36, and 221.86 MeV) were used for image reconstruction using the LM-MLEM algorithm. For reference, the simulated secondary-neutron depth profiles obtained from Geant4 simulations (as presented in Fig. 5) are overlaid on each reconstructed image, providing a qualitative basis for evaluating the spatial consistency between the reconstruction and the theoretical expectation. The reconstructed 2D images, obtained by setting the center of the PMMA phantom as the image space, successfully reflected the expected macroscopic secondary-neutron distributions. As illustrated in Fig. 6, the images clearly visualized the distinct distal fall-off of the secondary-neutron distribution near the proton Bragg peak. Most notably, as the incident proton energy increased, a proportional spatial shift of the neutron source position deeper into the phantom was clearly observed, which is consistent with the theoretical expectations.

However, the reconstructed images exhibited certain characteristics reflecting the constraints of the data acquisition.

Specifically, the spatial distributions appeared partially truncated along the peripheral regions, as neutrons originating from off-axis angles had escaped detection due to the current detector's limited geometric acceptance. Additionally, the total number of collected valid double-scatter events for each energy setting was restricted to a 400 – 1,000 range. While these event yields were sufficient to observe the relative shift of the Bragg peak, they inherently limited the overall absolute spatial resolution of the current imaging system.

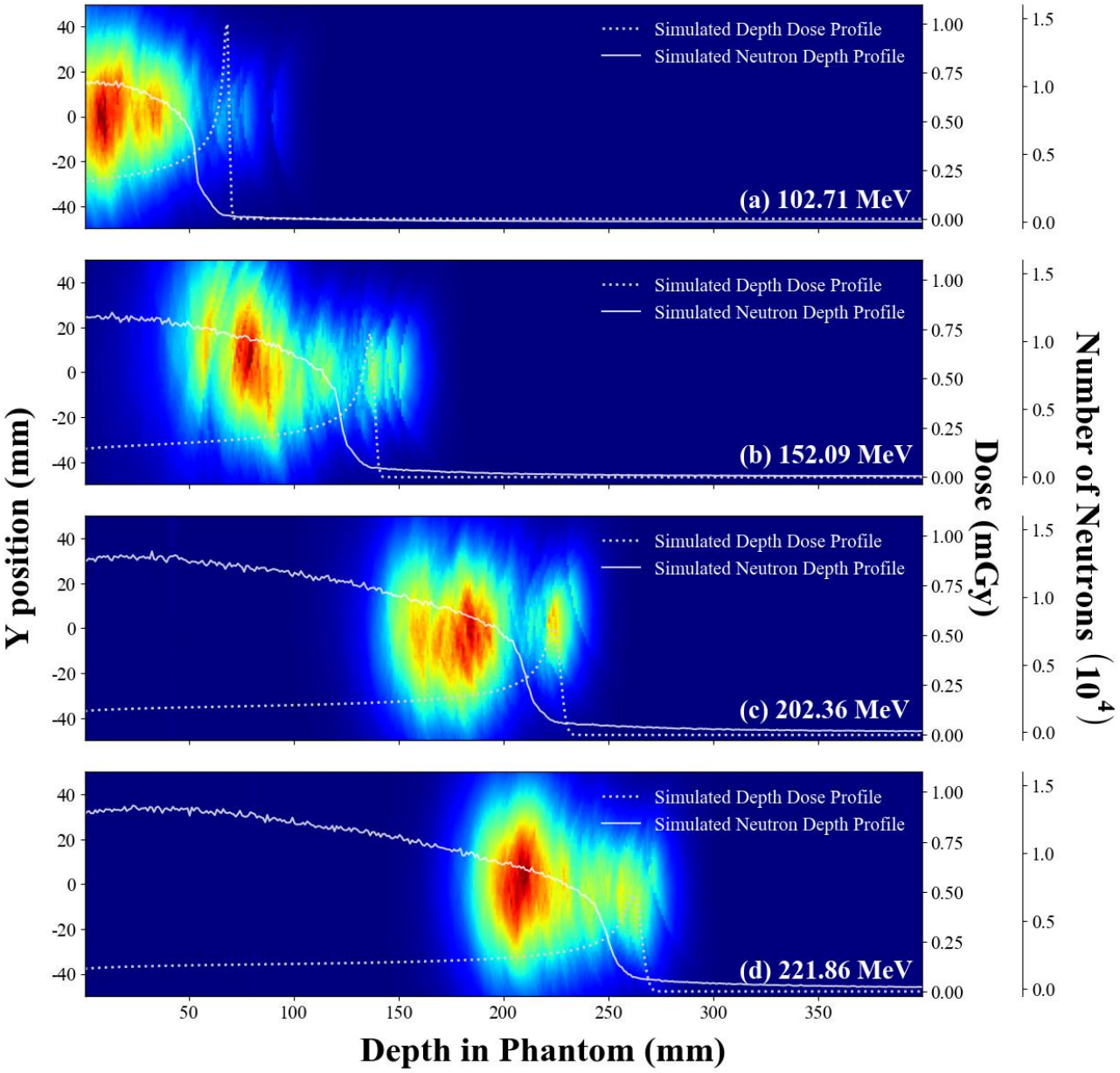

Fig. 6. Spatial distributions of secondary neutrons reconstructed by MLEM algorithm. The reconstructed 2D images are shown for proton beam energies of (a) 102.71 MeV, (b) 152.09 MeV, (c) 202.36 MeV, and (d) 221.86 MeV. Overlaid on each image are the simulated depth-dose profiles (dotted lines) and the simulated secondary-neutron depth profile for each proton beam energy (solid lines).

The reconstructed images accurately captured the neutron distribution and its spatial shift; however, achieving millimeter-level quantitative range verification with the current setup remains challenging. A major constraint was the temporal bottleneck introduced by the signal readout scheme. The active base employs a multiplexed readout, encoding the spatial position of the 4×4 pixel array into just four channels (+X, -X, +Y, -Y). Although this design significantly reduces the required number of channels, it inherently restricts data throughput, because every scattering event must be sequentially processed. This hardware constraint, compounded by a reliance on software-based filtering, severely limits the valid event yield; the resultant spatial blurring, moreover, likewise limits our capability to numerically define the exact distal fall-off position. Therefore, this study primarily focused on qualitative insights, leaving absolute range quantification for upgraded, high-yield detector systems to come. To address these limitations and achieve precise quantitative verification, future system iterations will implement a hardware-based time-of-flight (TOF) gate and integrate pulse-shape discrimination (PSD) techniques to actively reject the gamma-ray background. Furthermore, expanding the total detector volume will enhance geometric acceptance and statistical quality. Coupled with advanced image reconstruction algorithms—such as optimized statistical models or machine learning [31,32]—these hardware upgrades will yield superior spatial resolution. Overcoming these bottlenecks is particularly crucial for our ultimate clinical target: carbon ion therapy. Although the present proof-of-concept experiment was conducted using a proton beam, carbon ions generally produce higher yields of secondary neutrons with distinct forward-peaked angular distributions. Indeed, the successful qualitative localization of the Bragg peak in this proton study strongly suggests that an upgraded system will be highly effective for real-time range verification in the heavier ion therapy setting.

4. Conclusion

In this initial proof-of-concept study, we successfully demonstrated, for the first time, the feasibility of utilizing fast neutron scatter imaging for *in-vivo* proton range verification. By employing a prototype detector setup and LM-MLEM reconstruction, we accurately visualized the secondary-neutron distribution, dose fall-off, and energy-dependent spatial shifts of the Bragg peak within a PMMA phantom. However, the current system's image resolution and FOV were limited by a small detector size and a temporal bottleneck caused by the multiplexed readout and software-based filtering. To overcome these constraints, future upgrades will incorporate a hardware TOF gate, PSD, a larger detector volume, and machine-learning-based algorithms, ultimately paving the way for real-time dose verification. Furthermore, although this foundational work was conducted using a proton beam, our ultimate clinical objective is real-time range verification of carbon ion beams. Since carbon ions exhibit different secondary-neutron yields and kinematic characteristics relative to protons, future investigations will focus on evaluating the imager's performance in carbon beam environments, building upon the foundational proof-of-concept established in this study.

ACKNOWLEDGEMENTS

This study was supported by the National Research Foundation of Korea (NRF) funded by the Ministry of Science and ICT (RS-2023-00277188 and RS-2026-25547590) and by the Nuclear Safety Research Program through the Korea Foundation Of Nuclear Safety (KoFONS) using the financial resource granted by the Nuclear Safety and Security Commission (NSSC) of the Republic of Korea (RS-2025-02315183).

REFERENCES

[1] E. Hwang, P. Gorayski, H. Le et al., Particle therapy tumour outcomes: an updated systematic review. J. Med. Imag. Radiat. On. 64, 711–724 (2020). https://doi.org/10.1111/1754-9485.13021

[2] R. Mohan, A review of proton therapy – current status and future directions. Precis. Radiat. Oncol. 6, 164–176 (2022). https://doi.org/10.1002/pro6.1149

[3] A.L. Holtzman, K. Seidensaal, A. Iannalfi et al., Carbon ion radiotherapy: an evidence-based review and summary recommendations of clinical outcomes for skull-base chordomas and chondrosarcomas. Cancers 15, 5021 (2023). https://doi.org/10.3390/cancers15205021

[4] J. Zhang, Y. Lu, W. Hsi et al., Evaluation of proton therapy accuracy using a PMMA phantom and PET prediction module. Front. Oncol. 8, 523 (2018). https://doi.org/10.3389/fonc.2018.00523

[5] E. Debrot, D. Mundy, S. Guatelli et al., The dose magnifying glass quality assurance system for daily proton therapy range verification. Phys. Med. Biol. 66, 095001 (2021). https://doi.org/10.1088/1361-6560/abf1b9

[6] J.M. Pakela, A. Knopf, L. Dong et al., Management of motion and anatomical variations in charged particle therapy: past, present, and into the future. Front. Oncol. 12, 806153 (2022). https://doi.org/10.3389/fonc.2022.806153

[7] J. Schuemann, S. Dowdell, C. Grassberger et al., Site-specific range uncertainties caused by dose calculation algorithms for proton therapy. Phys. Med. Biol. 59, 4007–4031 (2014). https://doi.org/10.1088/0031-9155/59/15/4007

[8] M.S. Chacko, D. Wu, H.S. Grewal et al., Impact of beam-hardening corrections on proton relative stopping power estimates from single- and dual-energy CT. J. Appl. Clin. Med. Phys. 23, e13711 (2022). https://doi.org/10.1002/acm2.13711

[9] K. Parodi, J. Polf, In vivo range verification in particle therapy. Med. Phys. 45, e1036–e1050 (2018). https://doi.org/10.1002/mp.12960

[10] M. Moglioni, I. Rinaldi, S. Molinelli et al., In-vivo range verification analysis with in-beam PET data for patients treated with proton therapy at CNAO. Front. Oncol. 12, 929949 (2022). https://doi.org/10.3389/fonc.2022.929949

[11] Y. Yu, Z. Chen, Study on induced radioactivity of different materials in the proton therapy facility. J. Radiat. Prot. Res. 50, S95–S104 (2025). https://doi.org/10.14407/jrpr.2023.00535

[12] H. Matsumura, G. Yoshida, A. Toyoda et al., Radioactivation investigation for concrete in synchrotron-type proton therapy facilities. J. Radiat. Prot. Res. 50, S49–S60 (2025). https://doi.org/10.14407/jrpr.2023.00346

[13] C. Richter, G. Pausch, S. Barczyk et al., First clinical application of a prompt gamma based in vivo proton range verification system. Radiother. Oncol. 118, 232–237 (2016). https://doi.org/10.1016/j.radonc.2016.01.004

[14] A. Idrissi, L. Dedes, F. Roellinghoff et al., First experimental verification of prompt gamma imaging with carbon ion irradiation. Sci. Rep. 14, 25750 (2024). https://doi.org/10.1038/s41598-024-72870-6

[15] I. Meric, E. Alagoz, L. Hysing et al., A hybrid multi-particle approach to range assessment-based treatment verification in particle therapy. Sci. Rep. 13, 6709 (2023). https://doi.org/10.1038/s41598-023-33777-w

[16] S. Heo, S. Shin, C. Chung et al., Analysis of neutron production in passively scattered ion-beam therapy. Radiat. Prot. Dosim. 175, 297–303 (2017). https://doi.org/10.1093/rpd/ncw306

[17] M. Nandy, Secondary radiation in ion therapy and theranostics: a review. Front. Phys. 8, 598257 (2021). https://doi.org/10.3389/fphy.2020.598257

[18] J. Shin, H. Sim, S. Shin et al., MLEM-based image reconstruction algorithm for fast neutron scattering imaging. J. Instrum. 19, C12014 (2024). https://doi.org/10.1088/1748-0221/19/12/C12014

[19] Zhang M, Peng BD, Sheng L et al., Research of the system response of neutron double scatter imaging for MLEM reconstruction. Nucl. Instrum. Meth. A 775, 132–138 (2015). https://doi.org/10.1016/j.nima.2014.11.078

[20] L. Parra, H.H. Barrett, List-mode likelihood: EM algorithm and image quality estimation demonstrated on 2-D PET. IEEE Trans. Med. Imaging 17, 228–235 (1998). https://doi.org/10.1109/42.700734

[21] A.J. Reader, K. Erlandsson, M.A. Flower et al., Fast accurate iterative reconstruction for low-statistics positron volume imaging. Phys. Med. Biol. 43, 835–846 (1998). https://doi.org/10.1088/0031-9155/43/4/012

[22] H. Sim, Dissertation (Department of Applied Plasma and Quantum beam, Jeonbuk National University, 2026). https://www.riss.kr/link?id=T17370478

[23] S.B. Lee, J. Shin, D. Kim et al., Monte Carlo modeling and simulation of a passive treatment proton beam delivery system using a modulation wheel. J. Korean Phys. Soc. 56, 153–163 (2010). https://doi.org/10.3938/jkps.56.153

[24] J. Kim, Proton therapy facility project in national cancer center, Korea. J. Korean Phys. Soc. 43, S50–54 (2003).

[25] J. Kim, J. Kwon, J. Lee, Design of radiation shielding for proton therapy facility at the national cancer center in Korea. Radiat. Prot. Dosim. 115, 271–275 (2005). https://doi.org/10.1093/rpd/nci153

[26] V. Maradia, D. Meer, S. Bizzocchi et al., A new emittance selection system to maximize beam transmission for low-energy beams in cyclotron-based proton therapy facilities with gantry. Med. Phys. 48, 7613–7622 (2021). https://doi.org/10.1002/mp.15278

[27] International Atomic Energy Agency, Absorbed Dose Determination in External Beam Radiotherapy, Rev. 1, IAEA Technical Reports Series No. 398 (IAEA, Vienna, 2024) pp. 120–122. https://doi.org/10.61092/iaea.ve7q-y94k

[28] W. Hansen, D. Richter, Determination of light output function and angle dependent correlation for a stilbene crystal scintillation neutron spectrometer. Nucl. Instrum. Meth. A 476, 195–199 (2002). https://doi.org/10.1016/S0168-9002(01)01430-9

[29] C.Z. Jarlskog, H. Paganetti, Physics settings for using the Geant4 toolkit in proton therapy. IEEE Trans. Nucl. Sci. 55, 1018–1025 (2008). https://doi.org/10.1109/TNS.2008.922816

[30] W. Cho, M. Jung, J. Kim et al., Development of particle beam range verification technology based on high-energy prompt gamma-ray measurement. ETRI Final Report (2018). https://doi.org/10.22648/ETRI.2017.R.000336 (in Korean)

[31] S. Sato, K. Tanaka, J. Kataoka, ComptonNet: a direct reconstruction model for Compton camera. Appl. Phys. Lett. 124, 253702 (2024). https://doi.org/10.1063/5.0213950

[32] Z. Long, X. Jiang, A physics-constrained deep learning method for Compton cameras 3-D imaging. IEEE Trans. Nucl. Sci. 73, issue 1 (2026). https://doi.org/10.1109/TNS.2025.3624815